

Exploring the Synthesis of Alkali Metal Anti-perovskites

Kwangnam Kim,[¶] Yiliang Li,[¶] Ping-Chun Tsai, Fei Wang, Seoung-Bum Son, Yet-Ming Chiang,^{*} and Donald J. Siegel^{*}

Cite This: <https://doi.org/10.1021/acs.chemmater.1c02150>

Read Online

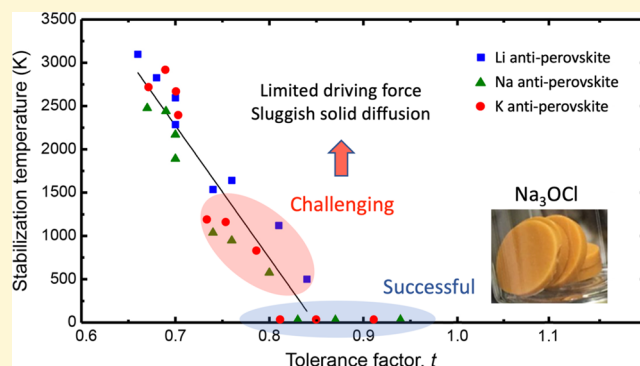
ACCESS |

Metrics & More

Article Recommendations

Supporting Information

ABSTRACT: The development of solid-state batteries has been slowed by limited understanding of the features that control ion mobility in solid electrolytes (SEs). In the case of anti-perovskite (AP) SE, lattice distortions have been proposed as one such controlling factor: APs that exhibit distortions of the octahedral building blocks are predicted to exhibit enhanced ionic mobility. Nevertheless, large distortions come at the cost of stability, implying a tradeoff between stability and ionic mobility. The present study combines theory and experiments to explore the synthesizability of several marginally stable APs predicted to exhibit high mobility for Li⁺, Na⁺, and K⁺. Density functional theory calculations, in combination with the quasi-harmonic approximation, were used to predict the free energy change, $\Delta G_r(T)$, for synthesis reactions involving 36 alkali metal-based APs, X_3AZ ($X = \text{Li, Na, or K}$; $A = \text{O, S, or Se}$; and $Z = \text{F, Cl, Br, or I}$). A linear correlation is observed between the degree of lattice distortion and the stabilization temperature, at which $\Delta G_r(T) = 0$. Hence, APs with the highest ionic mobility generally require the highest synthesis temperature. These data were used to guide experimental synthesis efforts of APs by estimating the temperatures above which a given AP is expected to be thermodynamically stable. Attempts were made to synthesize several AP compositions; overall, good agreement is obtained between experiments and computation. These data suggest that a compound's zero K decomposition energy is an efficient descriptor for predicting the ease and likelihood of synthesizing new SEs.



INTRODUCTION

Batteries are widely used for energy storage applications. Due to their high energy density, Li-ion batteries (LIBs) are pervasive in portable electronics and are making rapid inroads in electric vehicles. Na- and K-ion batteries are emerging, lower-cost alternatives to LIBs, with potential applications in large-scale stationary storage.^{1–3}

Independent of the application, safety is at the top of the list of desirable battery attributes. Safety issues are often traced to the use of flammable and volatile organic liquid electrolytes, which are commonly employed in LIBs.⁴ In principle, the development of inorganic solid electrolytes (SEs) could enhance safety while also allowing for the use of metal anodes, the latter of which exhibit higher energy densities than commonly used graphitic/intercalation anodes.^{5–7}

Many solids have been proposed as SEs, including $\text{Li}_7\text{La}_3\text{Zr}_2\text{O}_{12}$, $\text{Li}_6\text{PS}_3\text{Br}$, and $\text{Li}_{10}\text{GeP}_2\text{S}_{12}$.^{8–14} Despite their high ionic conductivities, essentially all SEs exhibit shortcomings such as poor interfacial stability and susceptibility to dendrite penetration.^{15–20} Consequently, the search for optimal SEs is an active area of research. The discovery of new SEs has been slowed, however, due to limited understanding of the factors that control fast ion transport in solids.^{21–26}

In the case of antiperovskite (AP) SEs, a prior study by some of the present authors revealed correlations between ion mobility, thermodynamic stability, and lattice distortions.^{27,28} These correlations were examined across a series of known and hypothetical APs with the formula X_3AZ ($X = \text{Li, Na, or K}$, $A = \text{O, S, or Se}$, and $Z = \text{F, Cl, Br, or I}$). The degree of lattice distortion in APs, which manifests as tilting of the alkali metal octahedra (and perturbations to the bond lengths/angles therein), is controlled by the composition and the associated ion packing efficiency, as quantified by the Goldschmidt tolerance factor $t = (R_X + R_Z) / [\sqrt{2}(R_X + R_A)]$, where R_X , R_A , and R_Z represent the respective ionic radii.²⁹ Importantly, the prior study identified a tradeoff between ionic mobility and low-temperature stability, the latter of which correlates with the degree of lattice distortions and, by extension, to the tolerance factor, t . This raises the question of whether the

Received: June 21, 2021

Revised: January 13, 2022

subset of APs predicted to exhibit exceptional ion mobilities, which are marginally-stable, can be synthesized.³⁰

Prior theoretical studies indicate that APs that are moderately unstable at low temperatures can be synthesized at higher temperatures, where thermal contributions enhance their stability. Li₃OCl represents one example, where density functional theory (DFT) calculations predict that this compound is thermodynamically unstable at zero K with respect to its respective Li chalcogenide and Li halide.^{31,32} However, later calculations indicated that Li₃OCl only becomes stable at temperatures above 500 K.^{33,34} Chen et al. suggested that this stabilization arises from vibrational entropy contributions from Li–Cl bonds; these bonds are predicted to be softer than those in the competing phase, LiCl.^{33,37} Experimentally, AP “Li₃OCl” samples have been found to be protonated.^{35,36} Similarly, it has been shown that APs with larger distortions are not only unstable at low *T* but also exhibit softer cation–framework-anion bonds,²⁷ suggesting a similar possibility for synthesis at elevated temperatures. Slow solid-state diffusion at ambient temperatures is also necessary to allow a phase which is stable only at high temperatures to avoid decomposition at lower temperatures³⁸ and thus be useful as a SE.

Along these lines, a prior study including some of the present authors compared the synthesis of Ag₃SI to Na₃SI.³⁹ Synthesis of the former compound has been reported in the literature,⁴⁰ while the latter is a new/hypothetical AP that was predicted to exhibit promising ionic mobility.²⁷ Based on DFT calculations, both compounds are predicted to be unstable at low temperatures and to become stable at high temperatures ranging from 600 to 1000 K.³⁹ Despite the similarity in their predicted phase stability, attempts to synthesize these compounds at high temperature were successful only for Ag₃SI. The difference in synthesis outcomes was attributed to the similarity of the anion sublattices of the reactants for Ag₃SI, Ag₂S and AgI, both of which adopt a BCC structure. This similarity was argued to facilitate solid-state diffusion and the anion mixing needed to form Ag₃SI. No such structural similarity was observed for the Na₃SI reactants, Na₂S and NaI; these structural differences were postulated to contribute to sluggish kinetics that hindered the formation of Na₃SI.

Building on these prior investigations, the present study combines theory and experiments to explore the thermal stabilization and synthesis of a wider series of alkali metal chalcogenide–halide APs. DFT calculations were used to predict several properties of these compounds. Melting temperatures of the APs were estimated using Lindemann’s law,⁴¹ and the free energies of the APs and their respective (precursor) chalcogenides and halides were estimated within the quasi-harmonic approximation (QHA). The stabilization temperature was determined by identifying the temperature at which the desired AP product becomes stable with respect to the chalcogenide and halide reactants. A linear correlation is observed between the degree of lattice distortion and the stabilization temperature. This implies that the most promising materials from the standpoint of ionic mobility require the highest synthesis temperatures. Consequently, these materials will also be the most metastable under ambient conditions. The stabilization temperature also increases exponentially with increasing metastability at zero K. Hence, simple total energy calculations (at *T* = 0 K)^{42,43} are a useful tool for assessing the complexity and likelihood of synthesizability.

The synthesis of 10 X₃AZ AP compositions (*X* = Li or Na; *A* = O or S; and *Z* = F, Cl, Br, or I) was explored experimentally, using solid-state reactions. Overall, the experimental synthesis efforts and computational predictions are in good agreement. For example, all three compounds Na₃OZ (*Z* = Cl, Br, or I) which were predicted to be stable at zero K were successfully synthesized. The most notable disagreement between theory and experiments occurred for Na₃SI. For this, AP synthesis at temperatures above the predicted stabilization temperature found no evidence of AP formation of the targeted AP. Furthermore, increases in the synthesis temperature were explored as a means to enhance kinetics and increase the thermodynamic driving force. However, these efforts were hampered by mass loss of (gaseous) halogens following the melting of the halides.

METHODS

Density Functional Theory. DFT calculations were performed with the Vienna *Ab initio* Simulation Package (VASP).⁴⁴ The Perdew–Burke–Ernzerhof⁴⁵ exchange–correlation functional was used in combination with the projector augmented wave method.^{46,47} The following valence electron configurations were adopted: 1s²2s¹ for Li, 3s¹ for Na, 3s²3p⁶4s¹ for K, 2s²2p⁴ for O, 3s²3p⁴ for S, 4s²4p⁴ for Se, 2s²2p⁵ for F, 3s²3p⁵ for Cl, 4s²4p⁵ for Br, and 5s²5p⁵ for I. The plane-wave basis included functions with kinetic energies up to 600 eV for Li- and Na-based compounds and up to 700 eV for K-containing compounds. It was observed that the K-based APs require higher cutoff energy to obtain converged elastic properties. The Brillouin zone was sampled on an 8 × 8 × 8 grid in the case of alkali halides (two atoms), a 6 × 6 × 6 grid for alkali chalcogenides (three atoms) and cubic APs (five atoms), and a 4 × 4 × 3 grid for quasi-orthorhombic APs (20 atoms), with a Γ -centered *k*-point mesh. These *k*-point sampling densities yielded energy convergence to within 1 meV/atom. Our tests showed that K APs require finer *k*-point meshes to achieve accurate elastic constants: a 15 × 15 × 15 grid for cubic K APs and a 6 × 6 × 4 grid for quasi-orthorhombic K APs were used when calculating elastic constants. The energy criterion for convergence of a self-consistent loop was set to 10^{−7} eV. The projection operators were evaluated in reciprocal space, and an additional support grid for the evaluation of the augmentation charges was used to calculate very accurate forces. The reported low-energy structures of the APs were adopted:^{27,28} compounds with large tolerance factors (*t* > 0.82) used cubic structures, otherwise a quasi-orthorhombic symmetry was adopted. These latter cases exhibit tilting and/or distortion of the alkali metal octahedra.²⁷

Phonon Calculations. The Gibbs free energies of compounds were calculated within the QHA. QHA is an extension of the harmonic approximation, which accounts for the thermal expansion of the lattice (*i.e.*, the dependence of the phonon modes on the cell volume is explicitly accounted for).³⁷ The Gibbs free energy *G* within the QHA is expressed as^{37,48}

$$G(T, p) = \min_V [F(T, V) + pV]$$

$$F(T, V) = E_0(V) + F_H(T, V)$$

where *E*₀ is the electronic energy at zero K (neglecting vibrational contributions), *F*_H is the vibrational free energy (including zero-point energy) of a harmonic system at a fixed temperature and volume, and min[*⋯*] indicates that *G* is a minimum with respect to variations in *V* volume *V* at a specified temperature, *T*, and pressure, *p*. The *pV* term is negligible for solids;⁴⁹ in this case, the free energy can be expressed as a function of *T* and *V* only. Equilibrium volumes were determined by fitting calculated total energy *versus* volume data to the Murnaghan equation of state (EOS).⁵⁰

In the harmonic approximation, phonon modes are calculated by diagonalizing a dynamical matrix derived from the harmonic phonon Hamiltonian.³⁷ The dynamical matrix is obtained from the

Hellmann–Feynman forces generated from small displacements of atoms in the supercell. This approach is commonly referred to as the direct method.⁵¹ The dynamical matrix of insulators having long-ranged Coulomb interactions is non-analytical; in these cases, the non-analytic component was evaluated separately and added to the analytical component of the dynamical matrix (which excludes Coulomb interactions).^{52–54} Using a partition function with discrete phonon microstates, the contribution of vibrational modes to the free energy can be expressed as⁵⁵

$$F_{\text{H}}(T, V) = k_{\text{B}}T \int_0^{\infty} d\omega g(\omega) \ln \left[2 \sinh \left(\frac{\hbar\omega}{2k_{\text{B}}T} \right) \right]$$

where k_{B} is the Boltzmann constant, \hbar is the Planck constant, and the integral is over all phonon frequencies ω within the density of states $g(\omega)$ for a fixed volume V . The presence of a small number of imaginary frequencies in some APs (*i.e.*, dynamical instability due to octahedral rotations),⁵⁶ if any, were neglected, following a previous analysis.³³

The phonon analysis was performed using PHONON software⁵⁷ using forces and properties obtained from DFT calculations. Hellmann–Feynman forces were calculated using enlarged supercells based on a $3 \times 3 \times 3$ replication with a single k -point (*i.e.*, Γ -point) for Li and Na cubic APs (135 atoms), Li and Na chalcogenides (324 atoms), and Li and Na halides (216 atoms), a $2 \times 2 \times 1$ replication with a Γ -centered $1 \times 1 \times 2$ k -point mesh for Li and Na quasi-orthorhombic APs (80 atoms), a $3 \times 3 \times 3$ replication with a Γ -centered $2 \times 2 \times 2$ k -point mesh for K cubic APs (135 atoms), a $2 \times 2 \times 1$ replication with a Γ -centered $2 \times 2 \times 2$ k -point mesh for K quasi-orthorhombic APs (80 atoms), and a $2 \times 2 \times 2$ replication with a Γ -centered $4 \times 4 \times 4$ k -point mesh for K chalcogenides (96 atoms) and K halides (64 atoms). These k -point sampling densities yielded energy convergence to within 1–2 meV/atom. Smaller simulation cell replications were used for K chalcogenides and halides due to their larger lattice constants and denser k -point meshes. Atomic displacements of 0.03, 0.05, and 0.20 Å were used for APs, chalcogenides, and halides, respectively. Born effective charges and static dielectric constants, which are needed to evaluate the non-analytical term in the dynamical matrix, were calculated from the Hessian matrix using density functional perturbation theory as implemented in VASP.

Thermodynamic Stability. The stabilization temperature T_{s} is defined as the temperature at which an AP that is predicted to be unstable at zero K²⁷ becomes stable. At temperatures above T_{s} , the free energy of the AP is lower than the (sum of) the free energies of competing phases. In the case of the APs, the competing phases are assumed to be the corresponding alkali metal chalcogenide and halide, which are often the reactants used to form the AP.^{27,31,32} Hence, for temperatures above the T_{s}

$$\Delta G_{\text{r}} = G_{\text{AP}} - (G_{\text{chalcogenide}} + G_{\text{halide}}) < 0$$

Additional details regarding the free energy calculations are presented in the Supporting Information (Figures S1–S3).

Melting Temperature. Lindemann's law treats melting as a vibrational instability and expresses the melting temperature as $T_{\text{m}} = c\langle M \rangle T_{\text{D}}^2 d^2$, where c is a constant, $\langle M \rangle$ is the average atomic mass, T_{D} is the Debye temperature, and d is a characteristic length ($d^3 = V_{\text{a}}$ is the average volume per atom).^{41,58} The Debye temperature is calculated from elastic properties as^{59,60}

$$T_{\text{D}} = \frac{2\pi\hbar}{k_{\text{B}}} \left[\frac{3n}{4\pi} \left(\frac{N_{\text{A}}\rho}{M} \right) \right]^{1/3} v_{\text{m}}$$

$$v_{\text{m}} = \left[\frac{1}{3} \left(\frac{2}{v_{\text{t}}^3} + \frac{1}{v_{\text{l}}^3} \right) \right]^{-1/3}$$

$$v_{\text{l}} = \left(\frac{B + \frac{4S}{3}}{\rho} \right)^{1/2}, \quad v_{\text{t}} = \left(\frac{S}{\rho} \right)^{1/2}$$

where n is the number of atoms in a unit cell, N_{A} is Avogadro's number, ρ is the density, M is the molecular weight, v_{m} is the average sound velocity, v_{l} and v_{t} are the longitudinal and transverse mode velocities, respectively, and B and S are the bulk and shear moduli, respectively. The Voigt⁶¹ and Reuss⁶² formulas estimate the theoretical maximum and minimum values of the moduli, respectively, using the stiffness tensor C_{ij} .⁶³ Given that the calculated Voigt bulk moduli were observed to be similar to those obtained from a fit to the Murnaghan EOS (see Table S1 in the Supporting Information), the present study adopted the Voigt expressions

$$B = [(C_{11} + C_{22} + C_{33}) + 2(C_{12} + C_{13} + C_{23})]/9$$

$$S = [(C_{11} + C_{22} + C_{33}) - (C_{12} + C_{13} + C_{23}) + 3(C_{44} + C_{55} + C_{66})]/15$$

These elastic properties were calculated using DFT. Finite differences were used for stiffness tensor calculations. Details regarding these calculations and the procedure for determining the constant c in Lindemann's relation are presented in the Supporting Information (Table S2).

Material Synthesis. APs with compositions X_3AZ ($X = \text{Li}$ or Na ; $A = \text{O}$ or S ; and $Z = \text{F}$, Cl , Br , or I), $\text{Li}_2(\text{OH})\text{Cl}$, and $\text{Li}_2(\text{OH})\text{Br}$ were prepared through solid-state reactions using Li_2O (Sigma-Aldrich, anhydrous, 99.5%), LiOH (Sigma-Aldrich, anhydrous, 99.5%), Na_2O (Sigma-Aldrich, anhydrous, 80%), Li_2S (Sigma-Aldrich, anhydrous, 99.9%), Na_2S (Sigma-Aldrich, anhydrous, 97%), and LiCl , LiBr , LiI , NaF , NaCl , NaBr , or NaI (each Sigma-Aldrich, anhydrous, 99.9%) as reactants. The starting materials were mixed and ground for 0.5–3 h in a high-energy ball mill (SPEX SamplePrep Mixer/Mill 8000 M) using a steel jar and steel milling balls and then hydraulically pressed at 60 MPa for ~ 2 min to form disc-shaped pellets of 0.5 in. diameter. Depending on the composition, pressed pellets were heat treated at temperatures in the range 320–900 °C, for 2–24 h in argon-filled gloveboxes with < 0.1 ppm O_2 and < 0.1 ppm H_2O . The ball mill was loaded with the starting material and sealed before milling and unloaded after milling, in the same glovebox atmosphere in order to minimize water absorption. Some variations from this procedure were also explored, as discussed in the Results and Discussion section. In one instance, a pre-synthesized AP powder of a different composition was used to attempt “seeding” of the AP phase. In another instance, a sealed quartz tube was used to prevent evaporative loss of molten alkali halide. In one experiment, the sample was heated under flowing argon in a quartz tube furnace. In all synthesis experiments, the crystalline phases present after heat treatment were characterized by *ex situ* powder X-ray diffraction (PXRD), using a PANalytical X'Pert Pro multipurpose diffractometer equipped with a $\text{Cu K}\alpha$ radiation source and an X'Celerator detector.

RESULTS AND DISCUSSION

Thermal Stabilization. Figure 1 shows a correlation between the calculated T_{s} and the tolerance factor across Li-, Na-, and K-based APs. These data, along with the predicted melting temperatures, are listed in Table 1. The predicted T_{s} for Li_3OCl is 500 K, which is similar to previous predictions (480 and 532 K).^{33,34} However, T_{s} for Li_3SI , predicted to be 1121 K here, does not agree with a previous prediction (520 K).³⁴ This difference can be traced to different crystal structures used in the calculations: ref 34 assumed cubic $Pm\bar{3}m$ symmetry, whereas the present study adopted a lower-energy orthorhombic ($Pnma$) structure. The latter structure exhibits lattice distortions in the form of octahedral tilting and is 9 meV/atom lower in energy than the cubic $Pm\bar{3}m$ phase.²⁷ Of the remaining 34 APs examined here, the T_{s} for two— Li_3OBr and Li_3OI —could not be predicted because the plot of ΔG versus T was always positive for the temperatures examined (see Figure S4 and text in the Supporting Information),

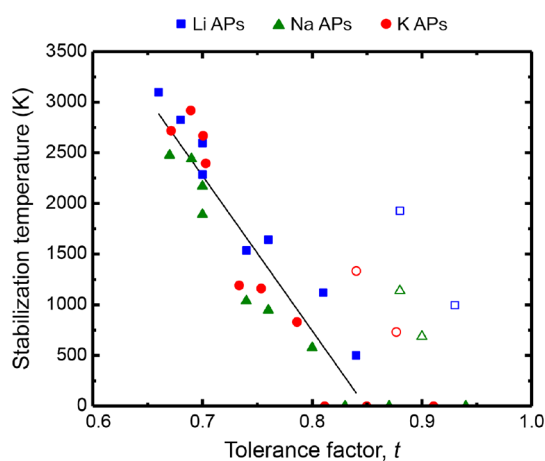


Figure 1. Correlation between the tolerance factor of APs, t , and their stabilization temperature, T_s . “F-centered” compounds are shown with open symbols. A linear fit is implemented excluding the F-centered subset and compounds that are stable at zero K.

suggesting that these phases are potentially intrinsically unstable.

The data in Figure 1 imply that synthesis at increasingly higher temperatures is needed to stabilize APs having a decreasing tolerance factor, t . As previously described, APs with smaller t have correspondingly larger lattice distortions.²⁷ Although located in a different range of t , the F-centered compounds, which have an F anion at the octahedron center (*i.e.*, the two anion species spontaneously swap sublattice positions upon relaxation),²⁷ also exhibit a similar trend. Indeed, like Li_3OCl , most of the model AP compounds are predicted to become stable at elevated temperatures due to thermal effects (*i.e.*, vibrational contributions to the enthalpy and entropy). Six compounds Na_3OCl , Na_3OBr , Na_3OI , K_3OCl , K_3OBr , and K_3OI are stable at zero K (*i.e.*, $T_s = 0$ K). Other factors being equal, it is generally desirable that T_s be as low as possible. A low T_s implies that synthesis should be achievable at lower temperatures. Moreover, the APs are envisioned as SEs to be used in batteries at near-ambient temperatures. APs synthesized above T_s might be kinetically stabilized at lower temperature³⁸ by use of an appropriate cooling schedule.^{11,34,64,65} In these cases, APs with a lower T_s

will exhibit a smaller thermodynamic driving force to decompose, potentially allowing for their persistence (and use) at ambient temperatures.

The predicted melting temperatures of the APs are listed in Table 1 and in Figure S5. Knowledge of the melting temperatures is helpful because melting can influence the accuracy with which T_s is predicted. More specifically, the present calculations assume that the reactants and products exist (at all T) as solid-state compounds that do not undergo polymorphic phase transformations, and the calculations do not account for melting or sublimation. These transformations change the slope of $G(T)$ and can therefore impact the predicted T_s . For example, the slope of $G(T)$ for the AP becomes steeper upon melting. If the AP melts below T_s , then T_s (as calculated using the above assumptions) will be an overestimate. APs in this category include (see Table 1) the sulfides, selenides, and the oxy-fluorides. Similarly, if one or both of the reactants melt below T_s , then the predicted T_s will underestimate the true T_s . This scenario also holds for most of the sulfides, selenides, and oxy-fluorides. Although these two effects—melting of the APs and melting of one or both of the chalcogenides and halides—have opposite effects on the prediction of T_s and their effects may partially cancel, it is likely that they contribute to uncertainty in the prediction of T_s . Unfortunately, properly accounting for the free energy of a liquid in DFT is a computationally expensive task and was not attempted. In addition, it is important to recognize that small errors in the calculated energies translate to large differences in temperature: a 25 meV error in energy is equivalent to a 300 K error in temperature. For these reasons, the T_s values predicted here are best interpreted as qualitative guides; although Table 1 lists T_s to three (or four) significant figures, such a high degree of precision is not justified by the approximations adopted here.

Figure 2 compares the T_s with the predicted energy barriers for long-range ion migration. Vacancy and interstitial dumbbell mechanisms are considered. These barriers were referred to as “limiting barriers” in a prior study.²⁷ Figure 2 shows that APs with the lowest barriers require high T_s , indicative of a tradeoff between mobility and stability.

As previously described, APs having lower T_s are expected to present advantages in terms of their ease of synthesis. On the

Table 1. Stabilization Temperatures, T_s , and Melting Temperatures, T_m , of the APs Examined Here and Their Corresponding Alkali Chalcogenides and Halides^a

Li APs	T_s (K)	T_m (K)	Na APs	T_s (K)	T_m (K)	K APs	T_s (K)	T_m (K)
Li_3OF	2827	460 (1711, 1121)	Na_3OF	2441	450 (1407, 1269)	K_3OF	2917	284 (1013, 1131)
Li_3OCl	500	555* (1711, 883)	Na_3OCl	0	528* (1407, 1075)	K_3OCl	0	364 (1013, 1044)
Li_3OBr		553* (1711, 823)	Na_3OBr	0	528* (1407, 1020)	K_3OBr	0	463 (1013, 1007)
Li_3OI		561 (1711, 742)	Na_3OI	0	513* (1407, 934)	K_3OI	0	451 (1013, 954)
Li_3SF	1928	461 (1645, 1121)	Na_3SF	1139	447 (1445, 1269)	K_3SF	1335	397 (1221, 1131)
Li_3SCl	2595	391 (1645, 883)	Na_3SCl	2169	368 (1445, 1075)	K_3SCl	2668	291 (1221, 1044)
Li_3SBr	1535	410 (1645, 823)	Na_3SBr	1037	383 (1445, 1020)	K_3SBr	1191	285 (1221, 1007)
Li_3SI	1121	431 (1645, 742)	Na_3SI	576	393 (1445, 934)	K_3SI	831	315 (1221, 954)
Li_3SeF	997	548 (1575, 1121)	Na_3SeF	688	570 (1148, 1269)	K_3SeF	733	381 (1073, 1131)
Li_3SeCl	3099	355 (1575, 883)	Na_3SeCl	2477	319 (1148, 1075)	K_3SeCl	2718	254 (1073, 1044)
Li_3SeBr	2287	367 (1575, 823)	Na_3SeBr	1891	338 (1148, 1020)	K_3SeBr	2396	275 (1073, 1007)
Li_3SeI	1641	398 (1575, 742)	Na_3SeI	946	360 (1148, 934)	K_3SeI	1162	302 (1073, 954)

^aMelting temperatures with an asterisk refer to experimental data.^{11,83} Values in parentheses are the experimental melting temperatures of the corresponding alkali chalcogenides and halides, respectively.⁹¹ APs with $T_s = 0$ are stable at zero K.^{27,28} Details regarding T_s for Li_3OZ ($Z = \text{Br}$ and I) are provided in the main text.

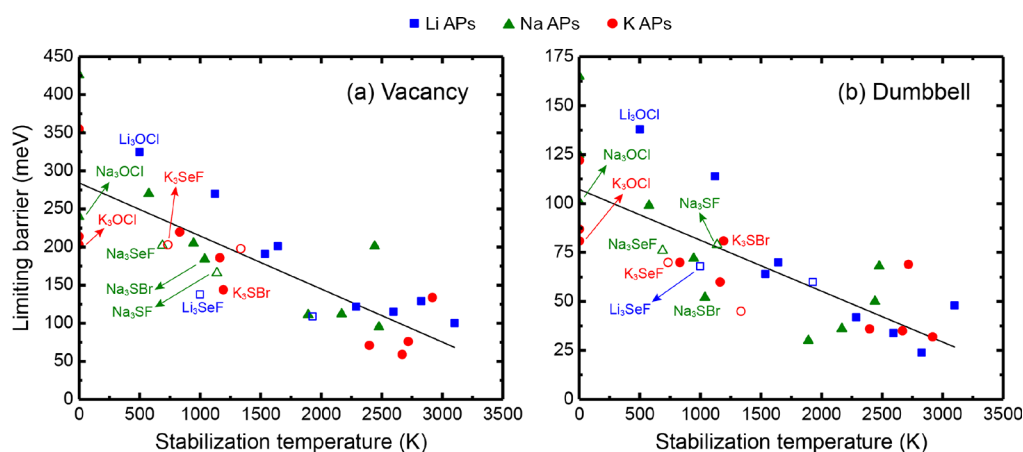


Figure 2. Comparison between the stabilization temperature T_s and the limiting barrier for APs for (a) vacancy and (b) dumbbell ion migration mechanisms. Noteworthy APs with relatively low T_s and limiting barriers are labeled. Empty symbols denote “F-centered” compounds. The limiting barriers were reported in refs 27 and 28.

other hand, APs with low limiting barriers are also desirable from the standpoint of their application as a SE. Based on the data in Figure 2, three compounds, Li_3SeF , Na_3SeF , and K_3SeF , exhibit both of these desirable features simultaneously. These APs have low limiting barriers for vacancy and dumbbell migration (138 and 68 meV for Li_3SeF , 202 and 76 meV for Na_3SeF , and 203 and 70 meV for K_3SeF). They also have moderate T_s ranging from 700 to 1000 K. A fourth compound, Na_3SI , also exhibits a favorable balance of stability and ionic mobility. This AP was discussed in two prior studies.^{27,39}

Figure 3 plots the relationship between T_s and the decomposition energy, E_d , of APs. Here, E_d is defined at zero

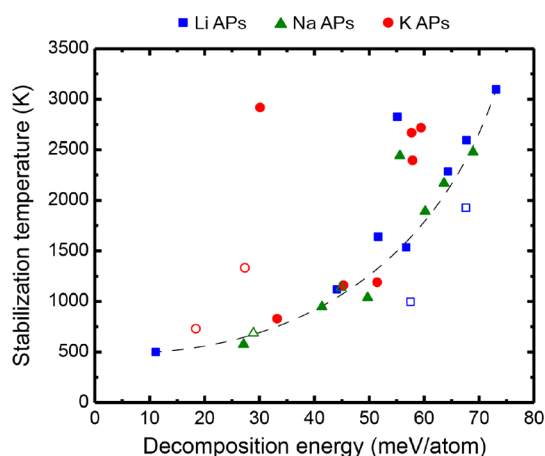


Figure 3. Stabilization temperatures T_s of AP compounds as a function of the decomposition energy at zero K. Empty symbols denote “F-centered” compounds. The dashed curve is a guide. Decomposition energies of APs are from refs 27 and 28.

K as the energy of a given AP relative to the summed energies of its respective alkali metal halide and chalcogenide: $E_d = E_{\text{AP}} - (E_{\text{halide}} + E_{\text{chalcogenide}})$. Alternatively, E_d may be interpreted as the energy above the convex hull, where the energy of the hull is taken as the sum $E_{\text{halide}} + E_{\text{chalcogenide}}$. APs with $E_d > 0$ are thus unstable to decomposition into the halide and chalcogenide. Because E_d is much less expensive to calculate than the free energies needed to evaluate T_s , it is helpful to know if and how E_d and T_s are correlated.

In a related analysis, Schmidt et al. investigated the stability of APs contained within the Materials Project (MP) database.⁴² For the subset of compounds that also had an ICSD number (it was assumed that these phases had been synthesized), 41% had $E_d > 0$. Of these, 63% were weakly unstable, defined as having $E_d < 50$ meV/atom. Emery and Wolverton also showed that among 83 unstable perovskite compounds reported in the literature, 58 (70%) had $E_d < 50$ meV/atom.⁴³ These data imply that weakly unstable compounds (with $E_d < 50$ meV/atom) have a reasonable probability of being synthesized. APs from the present study that fall under this category include Li_3OCl , Li_3OBr , Li_3SI , Na_3SF , Na_3SBr , Na_3SI , Na_3SeF , Na_3SeI , K_3OF , K_3SF , K_3SI , K_3SeF , and K_3SeI and the six previously mentioned compounds Na_3OCl , Na_3OBr , Na_3OI , K_3OCl , K_3OBr , and K_3OI that are stable at zero K (see Supporting Information for the list of E_d values in Table S3).

Figure 3 shows that T_s increases exponentially with increasing E_d . For $0 < E_d < 50$ meV/atom, T_s increases slowly, from roughly 500 to 1000 K. Entropic contributions at 1000 K in the AP with $\Delta S = 5$ J/mol·K can overcome a ~ 50 meV/atom difference in energy with competing phases at zero K.³⁸ For APs with $E_d > 50$ meV/atom, T_s increases much more rapidly, growing by approximately 2000 K as E_d increases from 50 to 70 meV/atom. Although in principle, these compounds could be synthesized—albeit at much higher temperatures—Schmidt et al.⁴² and Emery and Wolverton⁴³ both reported that experimental observations of these highly unstable phases are rare. These studies found that only 15% of APs and 11% of perovskites contained in computational databases (Materials Project and the Open Quantum Materials Database) had been synthesized. This suggests a diminishing likelihood for realizing these materials as E_d increases. APs in this “most unstable” category include Li_3OF , Li_3OI , Li_3SF , Li_3SCl , Li_3SBr , Li_3SeF , Li_3SeCl , Li_3SeBr , Li_3SeI , Na_3OF , Na_3SCl , Na_3SeCl , Na_3SeBr , K_3SCl , K_3SBr , K_3SeCl , and K_3SeBr .

Synthesis Experiments. In the Li-ion chalcogenide family, synthesis of four APs was attempted: Li_3OZ (where $Z = \text{F}, \text{Cl}, \text{or Br}$) and Li_3SI . Based on the calculated zero K stability (*i.e.*, decomposition energy in Table S3) or T_s , the most stable compounds among these are Li_3OCl (predicted to be stable at $T > 500$ K) and Li_3OBr . In attempting synthesis of Li_3OCl , X-ray diffraction (Table 2 and Figure S7a) revealed

Table 2. Experimental Synthesis Results Compared to Stabilization Temperature (T_s) Predictions from Computations^a

AP compound	predicted T_s (K)	experimental synthesis temperature (K)	AP phase observed?	X-ray diffraction observations
Li ₃ OF	2827	1073	no	final phases are the same as the reactant phases Li ₂ O and LiF; no detectable AP phase.
Li ₃ OCl	500	723–793	yes, but likely Li _{3-x} O _{1-x} H _x Cl	major phases after reaction are the same as reactants, Li ₂ O and LiCl, with minor amount of the AP phase. “Seeding” with pre-synthesized Na ₃ OCl AP powder did not result in significant amounts of the Li ₃ OCl AP phase; Na ₃ OCl decomposed to Na ₂ O and NaCl.
Li ₃ OBr	unstable at all temperatures explored	723–793	yes, but likely Li _{3-x} O _{1-x} H _x Br	major phases after reaction are reactant phases Li ₂ O and LiBr, an intermediate compound Li ₇ Br ₃ O ₂ , and a very small amount of the AP phase.
Li ₃ SI	1121	773–1173	no	final phases are the same as the reactant phases Li ₂ S and LiI; no detectable AP phase.
Na ₃ OCl	0	723	yes	cubic AP phases with space group $Pm\bar{3}m$ synthesized using reactants Na ₂ O and NaCl.
Na ₃ OBr	0	723	yes	cubic AP phases with space group $Pm\bar{3}m$ synthesized using reactants Na ₂ O and NaBr.
Na ₃ OI	0	783	yes	cubic AP phases with minor amounts of competing phases Na ₄ OI ₂ and Na ₅ OI ₆ .
Na ₃ SF	1139	773	no	final phases are the same as the reactant phases Li ₂ S and LiF; no detectable AP phase.
Na ₃ SI	576	883–1023	no	final phases are the same as the reactant phases Na ₂ S and NaI; no detectable AP phase. Results unchanged for duration of high-energy ball milling from 0.5 to 3 h and increased reaction temperature up to 1023 K. See also ref 38, Yin et al.
Na ₃ SBr	1037	773	no	final phases are the same as the reactant phases Na ₂ S and NaBr; no detectable AP phase.

^aFor each compound, the predicted stabilization and experimental synthesis temperatures are given. Whether the AP phase was observed and details of X-ray diffraction analysis are given. For all experiments, only anhydrous reactants were used, and all experiments were conducted in argon-filled gloveboxes with <0.1 ppm O₂ and <0.1 ppm H₂O.

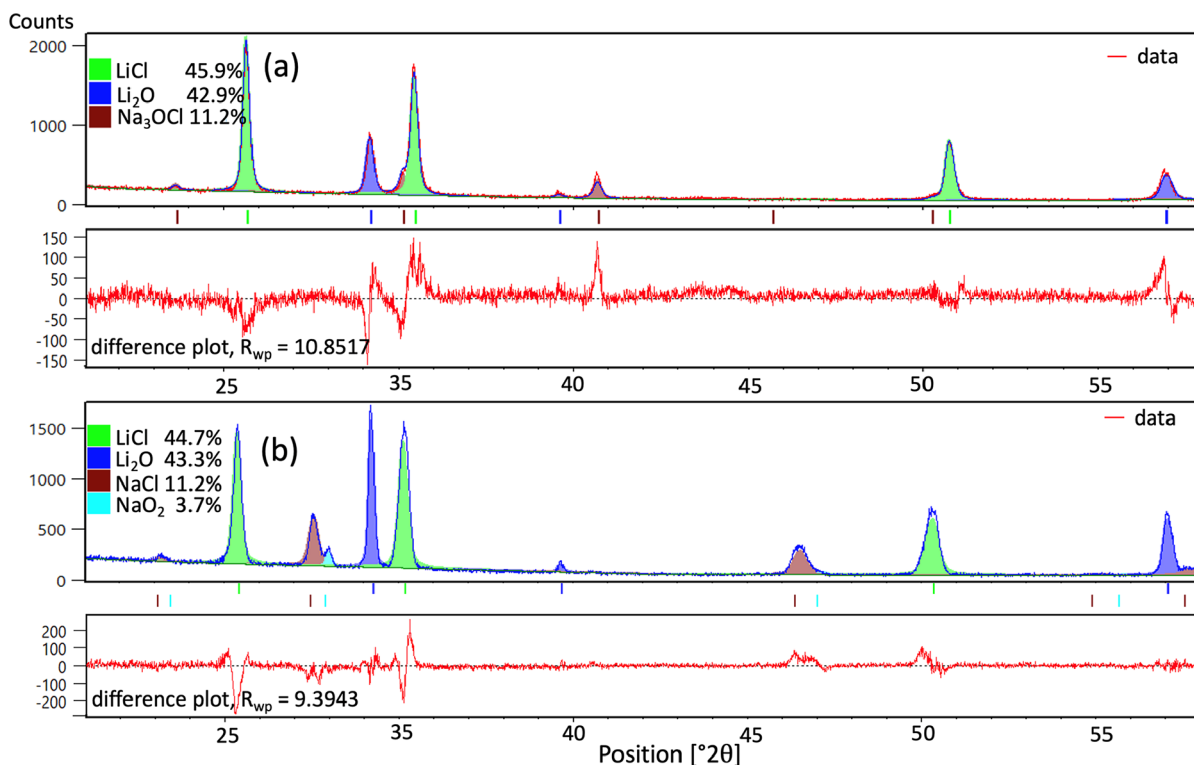


Figure 4. PXRD patterns of (a) pre-synthesized Na₃OCl AP powder mixed (at 20 wt % level) with milled Li₂O + LiCl precursors (80 wt %) (LiCl cubic $Fm\bar{3}m$ $a = 5.137$ Å, Li₂O cubic $Fm\bar{3}m$ $a = 4.603$ Å, and Na₃OCl cubic $Pm\bar{3}m$ $a = 4.481$ Å; $R_{wp} = 10.852$; and goodness of fit = 1.374) and (b) sample after pressing and heat treating at 723 K for 3 h. (LiCl cubic $Fm\bar{3}m$ $a = 5.170$ Å; Li₂O cubic $Fm\bar{3}m$ $a = 4.596$ Å, NaCl cubic $Fm\bar{3}m$ $a = 5.571$ Å, and Na₂O cubic $Fm\bar{3}m$ $a = 5.500$ Å; $R_{wp} = 9.39$; and goodness of fit = 1.462) The initially present Na₃OCl did not seed the crystallization of Li₃OCl APs; to the contrary, the starting Na₃OCl phase decomposed to Na₂O and NaCl in the presence of Li₂O and LiCl.

that the major phases after reacting for 24 h at 793 K are the reactant phases Li₂O and LiCl, with a small amount of the AP phase being detected. In attempting synthesis of Li₃OBr under the same temperature and time conditions, X-ray diffraction (Table 2 and Figure S7b) showed the presence of the reactant phases Li₂O and LiBr, an intermediate compound Li₇Br₃O₂, and only a small amount of the AP phase. Calculations have

shown that Li₃OCl reacts exothermically with H₂O.⁶⁶ Although Li₃OBr and Li₃OCl were claimed to have been successfully synthesized in earlier reports,^{67,68} Hanghofer et al.³⁶ showed that when the AP phase forms, it is protonated. A body of work including some present authors has found that a single phase of the AP structure is only obtained when the composition approaches the formula Li₂(OH)Cl or Li₂(OH)-

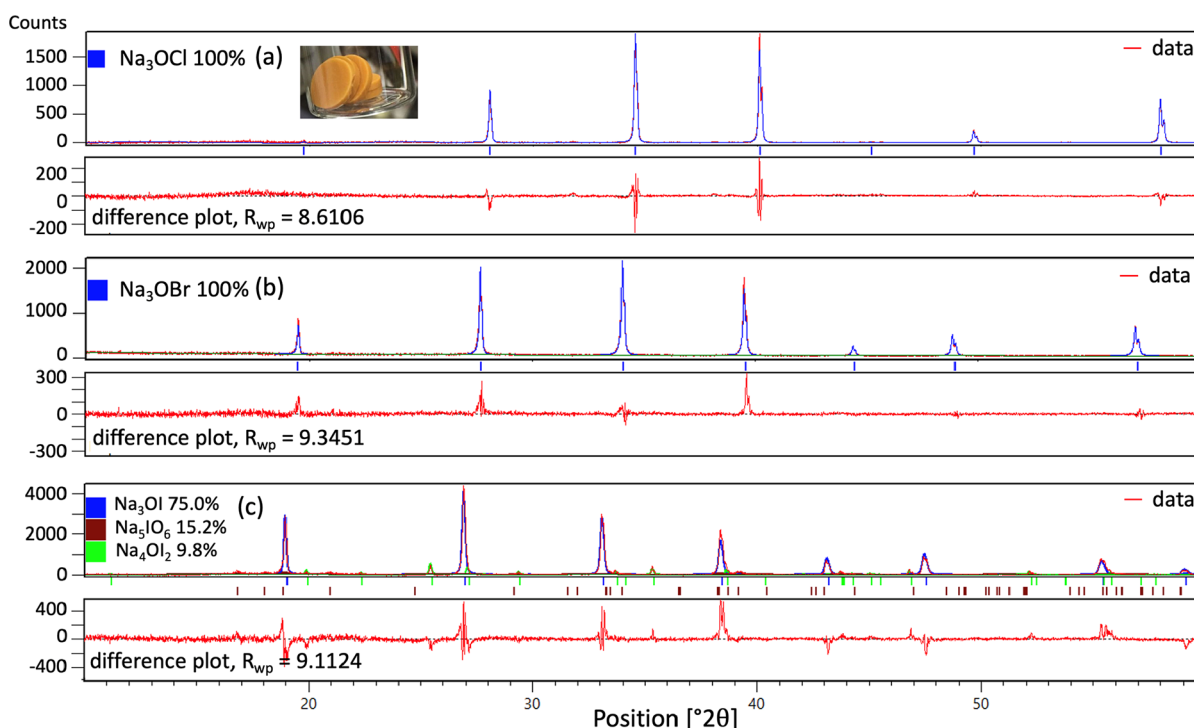


Figure 5. PXRD patterns at room temperature of the as-synthesized (a) Na_3OBr (cubic $Pm\bar{3}m$ $a = 4.566$ Å, $R_{\text{wp}} = 9.35$, and goodness of fit = 1.169), (b) Na_3OCl (cubic $Pm\bar{3}m$ $a = 4.492$ Å, $R_{\text{wp}} = 8.61$, and goodness of fit = 1.453), and (c) Na_3OI (cubic $Pm\bar{3}m$ $a = 4.689$ Å; Na_5OI_6 monoclinic $C2/m$ $a = 5.738$ Å, $b = 9.843$ Å, $c = 5.655$ Å, $\beta = 111.1^\circ$; Na_4OI_2 : tetragonal $I4/mmm$ $a = b = 4.660$ Å, $c = 15.957$ Å; $R_{\text{wp}} = 9.11$; and goodness of fit = 1.709). Na_3OCl and Na_3OBr show a high Rietveld refinement AP phase purity of >99%, while the AP phase purity of Na_3OI was found to be $\sim 80\%$ due to competing reactions which produced a small amount of secondary phases Na_4OI_2 ($\text{Na}_2\text{O} + 2\text{NaI} \rightarrow \text{Na}_4\text{OI}_2$) and Na_5OI_6 ($\text{Na}_2\text{O} + 6\text{NaI} \rightarrow \text{Na}_5\text{OI}_6 + 3\text{Na}$). The inset photograph shows densified and heat-treated Na_3OCl samples.

Br.^{35,36,66,69–78} It is difficult to completely prevent exposure to H_2O even when experiments are conducted in inert gas-filled gloveboxes.^{75,77} Rietveld refinement of XRD on the sample using reactants Li_2O and LiCl after ball milling shows LiCl and Li_2O constituting more than 98% by phase percentage. A small additional peak at 32.5° (Figure S8) matches with the major peak of the Li_2OHCl AP phase, indicating that a small amount of $\text{Li}_{3-x}(\text{OH}_x)\text{Cl}$ is produced during synthesis. Consistent with these expectations, synthesis using LiOH and Li halides as reagents resulted in single-phase OH AP analogues, namely, an orthorhombic $\text{Li}_2(\text{OH})\text{Cl}$ AP phase and a cubic $\text{Li}_2(\text{OH})\text{Br}$ AP phase at room temperature (Figure S9). We speculate that the AP phase found in small quantities in samples prepared using the anhydrous precursors may also be the OH analogue.

In agreement with these observations, using data from the Materials Project,⁷⁹ the calculated E_d for $\text{Li}_2(\text{OH})\text{Cl}$ with respect to LiOH and LiCl is 11 meV/atom, compared to $E_d = 30$ meV/atom for Li_3OCl . This indicates that $\text{Li}_2(\text{OH})\text{Cl}$ is more stable than Li_3OCl . In addition, Li_3OCl is predicted to react readily with H_2O via an exothermic reaction: $\text{Li}_3\text{OCl} + \text{H}_2\text{O} \rightarrow \text{Li}_2(\text{OH})\text{Cl} + \text{LiOH}$, with a -92 meV/atom reaction energy. This energy is similar to that of an earlier report⁶⁶ and adds additional support for the hygroscopic nature of Li_3OCl . Regarding Li_3OBr , the apparent preference for formation of Li_2OHBr (rather than Li_3OBr) observed experimentally is consistent with the present DFT calculations, which predict that Li_3OBr is unstable at all of the temperatures examined.

A further experimental exploration of the thermodynamic stability of the Li_3OCl phase was conducted, wherein Na_3OCl , demonstrated to be stable as discussed later, was used to “seed” the growth of Li_3OCl and lower or remove the nucleation

barriers. The use of seeds to lower the nucleation barrier for crystallization of a stable phase, and to induce crystallization of metastable phases, has been discussed by Parambil and Heng.⁸⁰ Pre-synthesized Na_3OCl AP powder was mixed (at 20 wt % level) with milled Li_2O and LiCl precursors (80 wt %), followed by pressing and heat treating at 723 K for 3 h. If Li_3OCl is thermodynamically stable, the presence of the Na_3OCl AP seed phase should assist the formation of Li_3OCl . Remarkably, not only were the starting phases LiCl and Li_2O still the main phases remaining after heat treatment but also the starting Na_3OCl phase was found to have decomposed to Na_2O and NaCl (Figure 4). This result suggests that the starting Na_3OCl may have been rendered unstable upon diffusive mixing of Li and Na and that pure Li_3OCl is unstable at the temperatures of these experiments (723–793 K).

Li_3SI is the next most stable composition of the Li -ion APs studied; it has a predicted T_s of 1121 K. X-ray diffraction (Table 2 and Figure S10) revealed only the starting reactant phases Li_2S and LiI , with no detectable APs or other intermediate compounds, after reacting for 12 h at temperatures of 773, 973, and 1173 K. As the highest attempted synthesis temperature is only slightly above the predicted T_s , the thermodynamic driving force for formation of the AP will be relatively small. Also, at 973 and 1173 K, which are above the LiI melting point, mass loss of LiI by evaporation was found to be severe (Figure S10).³⁹ It should be noted that the formation of Li_3SI reported in a recent study appears to be a mixture of Li_2S and LiI , and not the targeted AP.⁸¹ The XRD peaks of the sample in that work exactly match those of the Li_2S and LiI reactants in Figure S10.

Li_3OF and Li_3OI are predicted to be the least stable compositions of the Li-ion APs, for which synthesis was attempted. Li_3OF has a very high predicted T_s of 2827 K, above the melting temperatures of both reactants Li_2O and LiF (1711 and 1121 K, respectively). Accordingly, after reaction at 1073 K for 12 h, X-ray diffraction (Table 2 and Figure S11) revealed only a mixture of the starting phases Li_2O and LiF . Although we did not attempt to synthesize Li_3OI , its decomposition energy of 87.0 meV/atom is the highest among the 36 alkali APs investigated computationally,²⁷ suggesting that the Li_3OI AP would not have been produced either. It should be noted that the Na- and K-ions analogues, Na_3OI and K_3OI , are predicted to be stable at zero K (Table 1) and have been synthesized in previous work.^{82,83}

Turning now to the Na-ion APs, six Na-ion chalcogenide–halide Na_3AZ compositions were attempted: Na_3OZ (where $Z = \text{Cl}, \text{Br}, \text{or I}$) and Na_3SZ (where $Z = \text{F}, \text{Br}, \text{or I}$). All of the Na-ion oxy-halide compositions (Na_3OZ , $Z = \text{Cl}, \text{Br}, \text{or I}$) are predicted to be stable at zero K.²⁷ Consistent with these predictions, X-ray diffraction showed that these three AP compounds were readily synthesized and formed cubic AP phases with the space group $Pm\bar{3}m$ at room temperature (Figure 5), as synthesized in the literature.^{65,83–88} The synthesized samples of Na_3OCl and Na_3OBr showed a high Rietveld refinement AP phase purity of >99%, while the phase purity of Na_3OI was found to be ~80% due to competing reactions which produced a small amount of the secondary phases Na_4OI_2 ($\text{Na}_2\text{O} + 2\text{NaI} \rightarrow \text{Na}_4\text{OI}_2$) and Na_5OI_6 ($\text{Na}_2\text{O} + 6\text{NaI} \rightarrow \text{Na}_5\text{OI}_6 + 3\text{Na}$); see Supporting Information for detailed synthesis conditions and sample images in Figure S12. We also notice that Ahiavi et al. used a lower synthesis temperature around 200 °C for Na_3OX ($X = \text{Cl}, \text{Br}, \text{I}, \text{or BH}_4$) and achieved relative densities of 85% for Na_3OCl and 71% for Na_3OBr in the as-synthesized pellet.⁸⁸ The successful synthesis of Na_3OX ($X = \text{Cl}, \text{Br}, \text{or I}$) at this temperature is consistent with our computed results, showing that these APs are stable at 0 K. However, in our experiments, we used a higher sintering temperature of around 450 °C in order to achieve a higher relative density of 91% for Na_3OCl and 85% for Na_3OBr . Another reason for using higher temperature is to ensure that Na_2O_2 decomposes into Na_2O and O_2 .

Na_3SI is predicted to be stable at a moderate temperature of 576 K. However, after reaction at 923 K for 12 h, close to the melting point of NaI (934 K), X-ray diffraction revealed only the starting phases Na_2S and NaI , with no detectable APs or other intermediate compounds (Table 2 and Figure S13). The duration of high-energy ball milling was increased from 0.5 to 3 h in order to improve solid-state reaction kinetics, should it be rate-limiting. However, after heat-treating at 923 K for 12 h, only the starting reactant phases Na_2S and NaI were observed (Figure S13). Increasing the reaction temperature to 973 and 1023 K resulted in loss of NaI by evaporation (Figure S14), but the phases observed after cooling were still the same as the initial reactants, Na_2S and NaI (Figure S13).³⁹ An additional experiment was conducted in which the milled and pressed sample was heat-treated inside a sealed quartz tube to prevent evaporation. Here also, no AP phase was observed; a small amount of impurity phases was observed due to the reaction of the starting Na_2S and NaI with the quartz tube (Figure S15). In total, the present observations mirror those found in an earlier study by the present authors that compared the synthesis of Ag_3SI and Na_3SI .³⁹

Attempts to synthesize the Na_3SF and Na_3SBr AP phases, which have predicted T_s of 1139 and 1037 K, respectively, were conducted using the same synthesis procedure as for Na_3SI . However, here also, only the starting reactants Na_2S and NaF or NaBr were observed by X-ray diffraction after heat-treating for 24 h at 773 K (Table 2 and Figure S16). Recently, Fujii et al. synthesized APs under high pressure (5 GPa) and at high temperature (1000 °C), wherein F was observed at the center of the alkali metal octahedra (i.e., $X_3\text{FZ}$, where $X = \text{Li}$ and Na and $Z = \text{S}, \text{Se}, \text{and Te}$, excluding Li_3FS).⁸⁹ The Na_3FS phase was reported to exhibit an orthorhombic structure with lattice parameters similar to those predicted earlier by Kim and Siegel.²⁷ Nevertheless, the predicted stability of Na_3FS at 0 K as a function of pressure showed that Na_3FS remains unstable up to pressures of 20 GPa.⁸⁹ Consequently, it was argued that pressure and temperature both contribute to stabilizing Na_3SF during synthesis. Authors from the same group also synthesized APs having hydrogen at the octahedron centers (i.e., $X_3\text{HZ}$, where $X = \text{Li}$ and Na and $Z = \text{S}, \text{Se}, \text{and Te}$).⁹⁰

Discussion. Table 2 summarizes the experiments conducted to test the computational predictions of AP stability. In general, the agreement between theory and experiments is reasonable. All of the Na_3OZ ($Z = \text{Cl}, \text{Br}, \text{and I}$) compositions were predicted to be stable at zero K, and all were successfully synthesized as the targeted APs. Li_3OF , Li_3SI , Na_3SF , and Na_3SBr each have predicted T_s above or very near the maximum synthesis temperature used, and none of the four were observed to crystallize the AP phase. In the case of Li_3OCl and Li_3OBr , neither of the targeted APs were successfully synthesized, likely due to formation of the more stable hydroxyl analogues. DFT calculations confirm that Li_2OHCl is more stable than Li_3OCl . Although no calculations were performed on Li_2OHBr , calculations on Li_3OBr did not identify a temperature at which this compound becomes stable with respect to Li_2O and LiBr . The most notable discrepancy between theory and experiment occurred for Na_3SI . Here, the experimental synthesis temperatures are 293–447 K above the predicted stability temperature, yet no AP phase was observed. This result is consistent with a prior report, which argued that differences in the anion sublattices of the Na_2S and NaI reactants resulted in sluggish solid-state diffusion and a failure to form the AP.³⁹

Furthermore, our data suggest that computationally expensive predictions of stabilization temperatures may not be necessary to guide experimental synthesis efforts. Rather, knowledge of the zero K decomposition energies appears to be sufficient to classify hypothetical compounds into two categories: (1) compounds with $E_d \leq 50$ meV/atom, which are potentially synthesizable at moderate temperatures, and (2) compounds with $E_d > 50$ meV/atom, which require higher temperatures and whose formation is less likely.

CONCLUSIONS

APs have been proposed as promising SEs due to their high mobility for alkali metal cations. Nevertheless, prior work has predicted a tradeoff between an AP's ionic mobility and its thermodynamic stability: APs with greater mobility are less stable. The present study combines theory and experiments to explore the synthesizability of several marginally stable APs. DFT calculations, in combination with the QHA, were used to predict the free energy change, $\Delta G_r(T)$, for synthesis reactions involving 36 alkali metal-based APs, $X_3\text{AZ}$ ($X = \text{Li}, \text{Na}, \text{or K}$; $A = \text{O}, \text{S}, \text{or Se}$; and $Z = \text{F}, \text{Cl}, \text{Br}, \text{or I}$). A linear correlation is

observed between the degree of lattice distortion and the stabilization temperature, at which $\Delta G_r(T) = 0$. Hence, APs with the highest ionic mobility generally require the highest synthesis temperatures. These data were used to guide experimental synthesis efforts of APs by estimating the temperatures above which a given AP is expected to be thermodynamically stable. A compound's zero K decomposition energy was identified as an efficient descriptor for predicting the ease and likelihood of synthesizing new SEs, without the need for expensive phonon calculations.

The synthesis of several APs (X_3AZ , where $X = \text{Li}$ or Na , $A = \text{O}$ or S , and $Z = \text{F}$, Cl , Br , or I) was explored using solid-state reactions. Overall, the experimental synthesis efforts and computational predictions are in good agreement. Na_3OZ ($Z = \text{Cl}$, Br , or I) APs that were predicted to be stable at zero K were successfully synthesized from Na_2O and NaZ ($Z = \text{Cl}$, Br , or I). The hygroscopic nature of Li_3OCl and Li_3OBr results in the formation of hydrogenated analogues Li_2OHCl and Li_2OHBr , which is consistent with the predicted strong exothermic reaction between Li_3OCl and H_2O . Synthesis of Li_3OF , Li_3SI , Na_3SF , and Na_3SBr was not achieved and was attributed to the high T_s of these APs and resulting marginal thermodynamic driving force. The most notable discrepancy between theory and experiments occurs for Na_3SI . This compound was not formed even at temperatures 293–447 K above the predicted stabilization temperature. This observation is consistent with a prior study that attributed the difficulty in synthesizing Na_3SI to sluggish solid diffusion arising from mismatch in the anion sublattices of the Na_2S and NaI reactants.

■ ASSOCIATED CONTENT

SI Supporting Information

The Supporting Information is available free of charge at <https://pubs.acs.org/doi/10.1021/acs.chemmater.1c02150>.

Discussion on prediction of stabilization temperature; free energy and density of states of LiI; free energy data of APs, chalcogenides, and halides; energy above the convex hull of APs; predicted bulk and shear moduli of APs; discussion on prediction of melting temperature; energy above the convex hull of Li_3OBr and Li_3OI ; discussion on melting temperature; illustration for upper limit of stabilization temperature; decomposition energy of APs; XRD patterns of Li_2OHCl , Li_2OHBr , and related samples; XRD patterns of $\text{Li}_2\text{S} + \text{LiI}$ and $\text{Li}_2\text{O} + \text{LiF}$; and XRD patterns of $\text{Na}_2\text{S} + \text{NaI}$, $\text{Na}_2\text{S} + \text{NaF}$, and $\text{Na}_2\text{S} + \text{NaBr}$ (PDF)

■ AUTHOR INFORMATION

Corresponding Authors

Yet-Ming Chiang – Department of Materials Science and Engineering, Massachusetts Institute of Technology, Cambridge, Massachusetts 02139, United States; Joint Center for Energy Storage Research, University of Michigan, Ann Arbor, Michigan 48109-2125, United States; orcid.org/0000-0002-0833-7674; Phone: +1 (617) 253-6471; Email: ychiang@mit.edu

Donald J. Siegel – Mechanical Engineering Department, Materials Science & Engineering, Applied Physics Program, and Joint Center for Energy Storage Research, University of Michigan, Ann Arbor, Michigan 48109-2125, United States;

orcid.org/0000-0001-7913-2513; Phone: +1 (734) 764-4808; Email: djsiege@umich.edu

Authors

Kwangnam Kim – Mechanical Engineering Department, University of Michigan, Ann Arbor, Michigan 48109-2125, United States; Present Address: Lawrence Livermore National Laboratory, Livermore, California, 94550, United States; orcid.org/0000-0003-1149-1733

Yiliang Li – Department of Materials Science and Engineering, Massachusetts Institute of Technology, Cambridge, Massachusetts 02139, United States; orcid.org/0000-0002-1663-7968

Ping-Chun Tsai – Department of Materials Science and Engineering, Massachusetts Institute of Technology, Cambridge, Massachusetts 02139, United States; Department of Mechanical Engineering, National Taiwan University of Science and Technology, Taipei 10607, Taiwan

Fei Wang – Department of Materials Science and Engineering, Massachusetts Institute of Technology, Cambridge, Massachusetts 02139, United States

Seoung-Bum Son – Department of Materials Science and Engineering, Massachusetts Institute of Technology, Cambridge, Massachusetts 02139, United States

Complete contact information is available at:

<https://pubs.acs.org/10.1021/acs.chemmater.1c02150>

Author Contributions

[†]K.K. and Y.L. contributed equally to this work.

Notes

The authors declare no competing financial interest.

■ ACKNOWLEDGMENTS

This work was supported as part of the Joint Center for Energy Storage Research (JCESR), an Energy Innovation Hub funded by the U.S. Department of Energy, Office of Science, Basic Energy Sciences.

■ REFERENCES

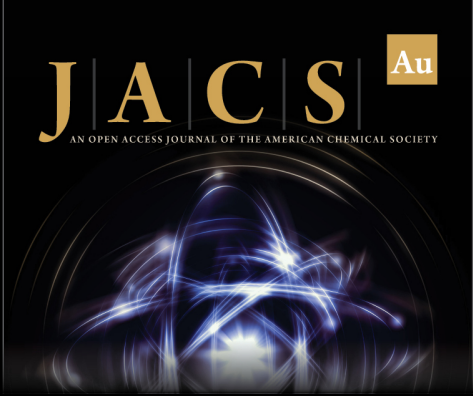
- (1) Kim, S.-W.; Seo, D.-H.; Ma, X.; Ceder, G.; Kang, K. Electrode Materials for Rechargeable Sodium-Ion Batteries: Potential Alternatives to Current Lithium-Ion Batteries. *Adv. Energy Mater.* **2012**, *2*, 710–721.
- (2) Eftekhari, A.; Jian, Z.; Ji, X. Potassium Secondary Batteries. *ACS Appl. Mater. Interfaces* **2017**, *9*, 4404–4419.
- (3) Kim, H.; Kim, J. C.; Bianchini, M.; Seo, D. H.; Rodriguez-Garcia, J.; Ceder, G. Recent Progress and Perspective in Electrode Materials for K-Ion Batteries. *Adv. Energy Mater.* **2018**, *8*, 1702384.
- (4) Roth, E. P.; Orendorff, C. J. How Electrolytes Influence Battery Safety. *Electrochem. Soc. Interface* **2012**, *21*, 45–49.
- (5) Monroe, C.; Newman, J. The Impact of Elastic Deformation on Deposition Kinetics at Lithium/Polymer Interfaces. *J. Electrochem. Soc.* **2005**, *152*, A396–A404.
- (6) Hu, Y.-S. Batteries: Getting Solid. *Nat. Energy* **2016**, *1*, 16042.
- (7) Albertus, P.; Babinec, S.; Litzelman, S.; Newman, A. Status and Challenges in Enabling the Lithium Metal Electrode for High-Energy and Low-Cost Rechargeable Batteries. *Nat. Energy* **2018**, *3*, 16–21.
- (8) Murugan, R.; Thangadurai, V.; Weppner, W. Fast Lithium Ion Conduction in Garnet-Type $\text{Li}_7\text{La}_3\text{Zr}_2\text{O}_{12}$. *Angew. Chem., Int. Ed.* **2007**, *46*, 7778–7781.
- (9) Deiseroth, H.-J.; Kong, S.-T.; Eckert, H.; Vannahme, J.; Reiner, C.; Zaiß, T.; Schlosser, M. $\text{Li}_x\text{PS}_x\text{X}$: A Class of Crystalline Li-Rich Solids with an Unusually High Li^+ Mobility. *Angew. Chem., Int. Ed.* **2008**, *47*, 755–758.

- (10) Kamaya, N.; Homma, K.; Yamakawa, Y.; Hirayama, M.; Kanno, R.; Yonemura, M.; Kamiyama, T.; Kato, Y.; Hama, S.; Kawamoto, K.; et al. A Lithium Superionic Conductor. *Nat. Mater.* **2011**, *10*, 682–686.
- (11) Zhao, Y.; Daemen, L. L. Superionic Conductivity in Lithium-Rich Anti-Perovskites. *J. Am. Chem. Soc.* **2012**, *134*, 15042–15047.
- (12) Richards, W. D.; Tsujimura, T.; Miara, L. J.; Wang, Y.; Kim, J. C.; Ong, S. P.; Uechi, I.; Suzuki, N.; Ceder, G. Design and Synthesis of the Superionic Conductor $\text{Na}_{10}\text{SnP}_2\text{S}_{12}$. *Nat. Commun.* **2016**, *7*, 11009.
- (13) Kato, Y.; Hori, S.; Saito, T.; Suzuki, K.; Hirayama, M.; Mitsui, A.; Yonemura, M.; Iba, H.; Kanno, R. High-Power All-Solid-State Batteries Using Sulfide Superionic Conductors. *Nat. Energy* **2016**, *1*, 16030.
- (14) Zhang, Z.; Shao, Y.; Lotsch, B.; Hu, Y.-S.; Li, H.; Janek, J.; Nazar, L. F.; Nan, C.-W.; Maier, J.; Armand, M.; et al. New Horizons for Inorganic Solid State Ion Conductors. *Energy Environ. Sci.* **2018**, *11*, 1945–1976.
- (15) Zhu, Y.; He, X.; Mo, Y. Origin of Outstanding Stability in the Lithium Solid Electrolyte Materials: Insights from Thermodynamic Analyses Based on First-Principles Calculations. *ACS Appl. Mater. Interfaces* **2015**, *7*, 23685–23693.
- (16) Richards, W. D.; Miara, L. J.; Wang, Y.; Kim, J. C.; Ceder, G. Interface Stability in Solid-State Batteries. *Chem. Mater.* **2016**, *28*, 266–273.
- (17) Wenzel, S.; Randau, S.; Leichtweiß, T.; Weber, D. A.; Sann, J.; Zeier, W. G.; Janek, J. Direct Observation of the Interfacial Instability of the Fast Ionic Conductor $\text{Li}_{10}\text{GeP}_2\text{S}_{12}$ at the Lithium Metal Anode. *Chem. Mater.* **2016**, *28*, 2400–2407.
- (18) Cheng, E. J.; Sharafi, A.; Sakamoto, J. Intergranular Li Metal Propagation through Polycrystalline $\text{Li}_{6.25}\text{Al}_{0.25}\text{La}_3\text{Zr}_2\text{O}_{12}$ Ceramic Electrolyte. *Electrochim. Acta* **2017**, *223*, 85–91.
- (19) Porz, L.; Swamy, T.; Sheldon, B. W.; Rettenwander, D.; Frömling, T.; Thaman, H. L.; Berendts, S.; Uecker, R.; Carter, W. C.; Chiang, Y. M. Mechanism of Lithium Metal Penetration through Inorganic Solid Electrolytes. *Adv. Energy Mater.* **2017**, *7*, 1701003.
- (20) Shen, F.; Dixit, M. B.; Xiao, X.; Hatzell, K. B. Effect of Pore Connectivity on Li Dendrite Propagation within LLZO Electrolytes Observed with Synchrotron X-Ray Tomography. *ACS Energy Lett.* **2018**, *3*, 1056–1061.
- (21) Ong, S. P.; Mo, Y.; Richards, W. D.; Miara, L.; Lee, H. S.; Ceder, G. Phase Stability, Electrochemical Stability and Ionic Conductivity of the $\text{Li}_{10\pm}\text{MP}_2\text{X}_{12}$ ($M = \text{Ge, Si, Sn, Al}$ or P , and $X = \text{O, S}$ or Se) Family of Superionic Conductors. *Energy Environ. Sci.* **2013**, *6*, 148–156.
- (22) Wang, Y.; Richards, W. D.; Ong, S. P.; Miara, L. J.; Kim, J. C.; Mo, Y.; Ceder, G. Design Principles for Solid-State Lithium Superionic Conductors. *Nat. Mater.* **2015**, *14*, 1026–1031.
- (23) Rong, Z.; Malik, R.; Canepa, P.; Sai Gautam, G.; Liu, M.; Jain, A.; Persson, K.; Ceder, G. Materials Design Rules for Multivalent Ion Mobility in Intercalation Structures. *Chem. Mater.* **2015**, *27*, 6016–6021.
- (24) Canepa, P.; Bo, S.-H.; Sai Gautam, G.; Key, B.; Richards, W. D.; Shi, T.; Tian, Y.; Wang, Y.; Li, J.; Ceder, G. High Magnesium Mobility in Ternary Spinel Chalcogenides. *Nat. Commun.* **2017**, *8*, 1759.
- (25) Kraft, M. A.; Culver, S. P.; Calderon, M.; Böcher, F.; Krauskopf, T.; Senyshyn, A.; Dietrich, C.; Zevalkin, A.; Janek, J.; Zeier, W. G. Influence of Lattice Polarizability on the Ionic Conductivity in the Lithium Superionic Argyrodites $\text{Li}_6\text{PS}_5\text{X}$ ($X = \text{Cl, Br, I}$). *J. Am. Chem. Soc.* **2017**, *139*, 10909–10918.
- (26) Mui, S.; Bachman, J. C.; Giordano, L.; Chang, H.-H.; Abernathy, D. L.; Bansal, D.; Delaire, O.; Hori, S.; Kanno, R.; Maglia, F.; et al. Tuning Mobility and Stability of Lithium Ion Conductors Based on Lattice Dynamics. *Energy Environ. Sci.* **2018**, *11*, 850–859.
- (27) Kim, K.; Siegel, D. J. Correlating Lattice Distortions, Ion Migration Barriers, and Stability in Solid Electrolytes. *J. Mater. Chem. A* **2019**, *7*, 3216–3227.
- (28) Kim, K. Computational Discovery of Solid Electrolytes for Batteries: Interfacial Phenomena and Ion Mobility. Ph.D. Thesis, University of Michigan, Ann Arbor, 2020.
- (29) Goldschmidt, V. M. Die Gesetze Der Krystallochemie. *Naturwissenschaften* **1926**, *14*, 477–485.
- (30) Dawson, J. A.; Famprikis, T.; Johnston, K. E. Anti-Perovskites for Solid-State Batteries: Recent Developments, Current Challenges and Future Prospects. *J. Mater. Chem. A* **2021**, *9*, 18746–18772.
- (31) Emly, A.; Kioupakis, E.; Van der Ven, A. Phase Stability and Transport Mechanisms in Antiperovskite Li_3OCl and Li_3OBr Superionic Conductors. *Chem. Mater.* **2013**, *25*, 4663–4670.
- (32) Zhang, Y.; Zhao, Y.; Chen, C. Ab Initio Study of the Stabilities of and Mechanism of Superionic Transport in Lithium-Rich Antiperovskites. *Phys. Rev. B: Condens. Matter Mater. Phys.* **2013**, *87*, 134303.
- (33) Chen, M.-H.; Emly, A.; Van der Ven, A. Anharmonicity and Phase Stability of Antiperovskite Li_3OCl . *Phys. Rev. B: Condens. Matter Mater. Phys.* **2015**, *91*, 214306.
- (34) Wang, Z.; Xu, H.; Xuan, M.; Shao, G. From Anti-Perovskite to Double Anti-Perovskite: Tuning Lattice Chemistry to Achieve Super-Fast Li^+ Transport in Cubic Solid Lithium Halogen-Chalcogenides. *J. Mater. Chem. A* **2017**, *6*, 73–83.
- (35) Li, Y.; Zhou, W.; Xin, S.; Li, S.; Zhu, J.; Lü, X.; Cui, Z.; Jia, Q.; Zhou, J.; Zhao, Y.; et al. Fluorine-Doped Antiperovskite Electrolyte for All-Solid-State Lithium-Ion Batteries. *Angew. Chem., Int. Ed.* **2016**, *55*, 9965–9968.
- (36) Hanghofer, I.; Redhammer, G. J.; Rohde, S.; Hanzu, I.; Senyshyn, A.; Wilkening, H. M. R.; Rettenwander, D. Untangling the Structure and Dynamics of Lithium-Rich Anti-Perovskites Envisaged as Solid Electrolytes for Batteries. *Chem. Mater.* **2018**, *30*, 8134–8144.
- (37) Van de Walle, A.; Ceder, G. The Effect of Lattice Vibrations on Substitutional Alloy Thermodynamics. *Rev. Mod. Phys.* **2002**, *74*, 11–45.
- (38) Sun, W.; Dacek, S. T.; Ong, S. P.; Hautier, G.; Jain, A.; Richards, W. D.; Gamst, A. C.; Persson, K. A.; Ceder, G. The Thermodynamic Scale of Inorganic Crystalline Metastability. *Sci. Adv.* **2016**, *2*, No. e1600225.
- (39) Yin, L.; Murphy, M.; Kim, K.; Hu, L.; Cabana, J.; Siegel, D. J.; Lapidus, S. H. Synthesis of Antiperovskite Solid Electrolytes: Comparing Li_3SI , Na_3SI , and Ag_3SI . *Inorg. Chem.* **2020**, *59*, 11244–11247.
- (40) Hull, S.; Keen, D. A.; Gardner, N. J. G.; Hayes, W. The Crystal Structures of Superionic Ag_3SI . *J. Phys.: Condens. Matter* **2001**, *13*, 2295–2316.
- (41) Lindemann, F. A. The Calculation of Molecular Vibration Frequencies. *Phys. Z.* **1910**, *11*, 609–612.
- (42) Schmidt, J.; Shi, J.; Borlido, P.; Chen, L.; Botti, S.; Marques, M. A. L. Predicting the Thermodynamic Stability of Solids Combining Density Functional Theory and Machine Learning. *Chem. Mater.* **2017**, *29*, 5090–5103.
- (43) Emery, A. A.; Wolverton, C. High-Throughput DFT Calculations of Formation Energy, Stability and Oxygen Vacancy Formation Energy of ABO_3 Perovskites. *Sci. Data* **2017**, *4*, 170153.
- (44) Kresse, G.; Furthmüller, J. Efficient Iterative Schemes for Ab Initio Total-Energy Calculations Using a Plane-Wave Basis Set. *Phys. Rev. B: Condens. Matter Mater. Phys.* **1996**, *54*, 11169–11186.
- (45) Perdew, J. P.; Burke, K.; Ernzerhof, M. Generalized Gradient Approximation Made Simple. *Phys. Rev. Lett.* **1996**, *77*, 3865–3868.
- (46) Blöchl, P. E. Projector Augmented-Wave Method. *Phys. Rev. B: Condens. Matter Mater. Phys.* **1994**, *50*, 17953–17979.
- (47) Kresse, G.; Joubert, D. From Ultrasoft Pseudopotentials to the Projector Augmented-Wave Method. *Phys. Rev. B: Condens. Matter Mater. Phys.* **1999**, *59*, 1758–1775.
- (48) Skelton, J. M.; Tiana, D.; Parker, S. C.; Togo, A.; Tanaka, I.; Walsh, A. Influence of the Exchange-Correlation Functional on the Quasi-Harmonic Lattice Dynamics of II-VI Semiconductors. *J. Chem. Phys.* **2015**, *143*, 064710.


- (49) Ong, S. P.; Wang, L.; Kang, B.; Ceder, G. Li–Fe–P–O₂ Phase Diagram from First Principles Calculations. *Chem. Mater.* **2008**, *20*, 1798–1807.
- (50) Murnaghan, F. D. The Compressibility of Media under Extreme Pressures. *Proc. Natl. Acad. Sci. U.S.A.* **1944**, *30*, 244–247.
- (51) Parlinski, K.; Li, Z. Q.; Kawazoe, Y. First-Principles Determination of the Soft Mode in Cubic ZrO₂. *Phys. Rev. Lett.* **1997**, *78*, 4063–4066.
- (52) Pick, R. M.; Cohen, M. H.; Martin, R. M. Microscopic Theory of Force Constants in the Adiabatic Approximation. *Phys. Rev. B: Solid State* **1970**, *1*, 910–920.
- (53) Detraux, F.; Ghosez, P.; Gonze, X. Long-Range Coulomb Interaction in ZrO₂. *Phys. Rev. Lett.* **1998**, *81*, 3297.
- (54) Parlinski, K.; Li, Z. Q.; Kawazoe, Y. Parlinski, Li, and Kawazoe Reply. *Phys. Rev. Lett.* **1998**, *81*, 3298.
- (55) Maradudin, A. A.; Montroll, E. W.; Weiss, G. H. *Theory of Lattice Dynamics in the Harmonic Approximation*, 2nd ed.; Academic Press: New York, 1971.
- (56) Zinenko, V. I.; Zamkova, N. G. Lattice Dynamics of Antiperovskite Structure Compounds A₃OX (A = Na, K; X = Cl, Br). *Ferroelectrics* **2002**, *265*, 23–29.
- (57) Parlinski, K. *PHONON Software*, Kraków, 2013.
- (58) Pines, D. *Elementary Excitations in Solids*; CRC Press: Boca Raton, 2018.
- (59) Anderson, O. L. A Simplified Method for Calculating the Debye Temperature from Elastic Constants. *J. Phys. Chem. Solids* **1963**, *24*, 909–917.
- (60) Schreiber, E.; Anderson, O. L.; Soga, N. *Elastic Constants and Their Measurements*; McGraw-Hill: New York, 1973.
- (61) Voigt, W. *Lehrbuch Der Kristallphysik*; Taubner: Leipzig, 1928.
- (62) Reuss, A. Berechnung Der Fließgrenze von Mischkristallen Auf Grund Der Plastizitätsbedingung Für Einkristalle. *J. Appl. Math. Mech.* **1929**, *9*, 49–58.
- (63) Ravindran, P.; Fast, L.; Korzhavyi, P. A.; Johansson, B.; Wills, J.; Eriksson, O. Density Functional Theory for Calculation of Elastic Properties of Orthorhombic Crystals: Application to TiSi₂. *J. Appl. Phys.* **1998**, *84*, 4891.
- (64) Kagawa, F.; Oike, H. Quenching of Charge and Spin Degrees of Freedom in Condensed Matter. *Adv. Mater.* **2017**, *29*, 1601979.
- (65) Jansen, M. Volume Effect or Paddle-Wheel Mechanism - Fast Alkali-Metal Ionic Conduction in Solids with Rotationally Disordered Complex Anions. *Angew. Chem., Int. Ed.* **1991**, *30*, 1547–1558.
- (66) Dawson, J. A.; Attari, T. S.; Chen, H.; Emge, S. P.; Johnston, K. E.; Islam, M. S. Elucidating Lithium-Ion and Proton Dynamics in Anti-Perovskite Solid Electrolytes. *Energy Environ. Sci.* **2018**, *11*, 2993–3002.
- (67) Lü, X.; Howard, J. W.; Chen, A.; Zhu, J.; Li, S.; Wu, G.; Dowden, P.; Xu, H.; Zhao, Y.; Jia, Q. Antiperovskite Li₃OCl Superionic Conductor Films for Solid-State Li-Ion Batteries. *Adv. Sci.* **2016**, *3*, 1500359.
- (68) Zhu, J.; Li, S.; Zhang, Y.; Howard, J. W.; Lü, X.; Li, Y.; Wang, Y.; Kumar, R. S.; Wang, L.; Zhao, Y. Enhanced Ionic Conductivity with Li₇O₂Br₃ Phase in Li₃OBr Anti-Perovskite Solid Electrolyte. *Appl. Phys. Lett.* **2016**, *109*, 101904.
- (69) Howard, J.; Hood, Z. D.; Holzwarth, N. A. W. Fundamental Aspects of the Structural and Electrolyte Properties of Li₂OHCl from Simulations and Experiment. *Phys. Rev. Mater.* **2017**, *1*, 1–13.
- (70) Song, A. Y.; Turcheniuk, K.; Leisen, J.; Xiao, Y.; Meda, L.; Borodin, O.; Yushin, G. Understanding Li-Ion Dynamics in Lithium Hydroxychloride (Li₂OHCl) Solid State Electrolyte via Addressing the Role of Protons. *Adv. Energy Mater.* **2020**, *10*, 1903480.
- (71) Wang, F.; Evans, H. A.; Kim, K.; Yin, L.; Li, Y.; Tsai, P.-C.; Liu, J.; Lapidus, S. H.; Brown, C. M.; Siegel, D. J.; et al. Dynamics of Hydroxyl Anions Promotes Lithium Ion Conduction in Antiperovskite Li₂OHCl. *Chem. Mater.* **2020**, *32*, 8481–8491.
- (72) Baurlage, H.; Jacobs, H. Ungewöhnliche Koordinationspolyeder Um Sauerstoff in Li₄Cl(OH)₃. *Z. Anorg. Allg. Chem.* **1994**, *620*, 471–474.
- (73) Friese, K.; Hönnerscheid, A.; Jansen, M. Crystal Structure Determination of Systematically Intergrown Compounds: Li₅(OH)₂Br₃ and Li₂(OH)Br. *Z. Kristallogr.—Cryst. Mater.* **2003**, *218*, 536–541.
- (74) Schwering, G.; Hönnerscheid, A.; van Wüllen, L.; Jansen, M. High Lithium Ionic Conductivity in the Lithium Halide Hydrates Li_{3-n}(OH_n)Cl (0.83 ≤ n ≤ 2) and Li_{3-n}(OH_n)Br (1 ≤ n ≤ 2) at Ambient Temperatures. *ChemPhysChem* **2003**, *4*, 343–348.
- (75) Zhang, J.; Han, J.; Zhu, J.; Lin, Z.; Braga, M. H.; Daemen, L. L.; Wang, L.; Zhao, Y. High Pressure-High Temperature Synthesis of Lithium-Rich Li₃O(Cl, Br) and Li_{3-x}Ca_{x/2}OCl Anti-Perovskite Halides. *Inorg. Chem. Commun.* **2014**, *48*, 140–143.
- (76) Hood, Z. D.; Wang, H.; Pandian, A. S.; Keum, J. K.; Liang, C. Li₂OHCl Crystalline Electrolyte for Stable Metallic Lithium Anodes. *J. Am. Chem. Soc.* **2016**, *138*, 1768–1771.
- (77) Li, S.; Zhu, J.; Wang, Y.; Howard, J. W.; Lü, X.; Li, Y.; Kumar, R. S.; Wang, L.; Daemen, L. L.; Zhao, Y. Reaction Mechanism Studies towards Effective Fabrication of Lithium-Rich Anti-Perovskites Li₃OX (X = Cl, Br). *Solid State Ionics* **2016**, *284*, 14–19.
- (78) Braga, M. H.; Murchison, A. J.; Ferreira, J. A.; Singh, P.; Goodenough, J. B. Glass-Amorphous Alkali-Ion Solid Electrolytes and Their Performance in Symmetrical Cells. *Energy Environ. Sci.* **2016**, *9*, 948–954.
- (79) Jain, A.; Ong, S. P.; Hautier, G.; Chen, W.; Richards, W. D.; Dacek, S.; Cholia, S.; Gunter, D.; Skinner, D.; Ceder, G.; et al. Commentary: The Materials Project: A Materials Genome Approach to Accelerating Materials Innovation. *APL Mater.* **2013**, *1*, 011002.
- (80) Parambil, J. V.; Heng, J. Y. Y. Seeding in Crystallisation. In *Engineering Crystallography: From Molecule to Crystal to Functional Form*; Roberts, K. J., Docherty, R., Tamura, R., Eds.; NATO Science for Peace and Security Series A: Chemistry and Biology; Springer Netherlands: Dordrecht, 2017; pp 235–245.
- (81) Park, M.-h.; Rajagopal, R.; Ryu, K.-S. Electrochemical Performance of the Mixed Solid Electrolyte (100-x)Li₃SI-XLi₆PS₅Cl (x = 0, 10, 20, and 30) for All-Solid-State Lithium Batteries. *J. Power Sources* **2021**, *501*, 230031.
- (82) Sitta, S.; Hippler, K.; Vogt, P.; Sabrowsky, H. Crystal Structure of K₃OI. *Z. Kristallogr.* **1991**, *196*, 193–196.
- (83) Wang, Y.; Wang, Q.; Liu, Z.; Zhou, Z.; Li, S.; Zhu, J.; Zou, R.; Wang, Y.; Lin, J.; Zhao, Y. Structural Manipulation Approaches towards Enhanced Sodium Ionic Conductivity in Na-Rich Anti-perovskites. *J. Power Sources* **2015**, *293*, 735–740.
- (84) Hippler, K.; Sitta, S.; Vogt, P.; Sabrowsky, H. Structure of Na₃OCl. *Acta Crystallogr., Sect. C: Cryst. Struct. Commun.* **1990**, *46*, 736–738.
- (85) Nguyen, H.; Hy, S.; Wu, E.; Deng, Z.; Samiee, M.; Yersak, T.; Luo, J.; Ong, S. P.; Meng, Y. S. Experimental and Computational Evaluation of a Sodium-Rich Anti-Perovskite for Solid State Electrolytes. *J. Electrochem. Soc.* **2016**, *163*, A2165–A2171.
- (86) Zhu, J.; Wang, Y.; Li, S.; Howard, J. W.; Neuefeind, J.; Ren, Y.; Wang, H.; Liang, C.; Yang, W.; Zou, R.; et al. Sodium Ion Transport Mechanisms in Antiperovskite Electrolytes Na₃OBr and Na₄OI₂: An *In Situ* Neutron Diffraction Study. *Inorg. Chem.* **2016**, *55*, 5993–5998.
- (87) Sun, Y.; Wang, Y.; Liang, X.; Xia, Y.; Peng, L.; Jia, H.; Li, H.; Bai, L.; Feng, J.; Jiang, H.; et al. Rotational Cluster Anion Enabling Superior Conductivity in Sodium-Rich Antiperovskite Na₃OBH₄. *J. Am. Chem. Soc.* **2019**, *141*, 5640–5644.
- (88) Ahiavi, E.; Dawson, J. A.; Kudu, U.; Courty, M.; Islam, M. S.; Clemens, O.; Masquelier, C.; Famprikis, T. Mechanochemical Synthesis and Ion Transport Properties of Na₃OX (X = Cl, Br, I and BH₄) Antiperovskite Solid Electrolytes. *J. Power Sources* **2020**, *471*, 228489.
- (89) Fujii, S.; Gao, S.; Tassel, C.; Zhu, T.; Broux, T.; Okada, K.; Miyahara, Y.; Kuwabara, A.; Kageyama, H. Alkali-Rich Antiperovskite M₃FCh (M = Li, Na; Ch = S, Se, Te): The Role of Anions in Phase Stability and Ionic Transport. *J. Am. Chem. Soc.* **2021**, *143*, 10668–10675.
- (90) Gao, S.; Broux, T.; Fujii, S.; Tassel, C.; Yamamoto, K.; Xiao, Y.; Oikawa, I.; Takamura, H.; Ubukata, H.; Watanabe, Y.; et al. Hydride-

Based Antiperovskites with Soft Anionic Sublattices as Fast Alkali Ionic Conductors. *Nat. Commun.* **2021**, *12*, 201.


(91) Rumble, J. R. *CRC Handbook of Chemistry and Physics*, 99th ed.; CRC Press: Boca Raton, 2018.




JACS Au
AN OPEN ACCESS JOURNAL OF THE AMERICAN CHEMICAL SOCIETY



Editor-in-Chief
Prof. Christopher W. Jones
Georgia Institute of Technology, USA

Open for Submissions 

pubs.acs.org/jacsau  ACS Publications
Most Trusted. Most Cited. Most Read.